

**University of Massachusetts Amherst**

---

**From the Selected Works of Thomas J. Lardner**

---

1990

## Use of the Microindentation Technique for Determining Interfacial Fracture Energy

Thomas J. Lardner, *University of Massachusetts - Amherst*

L. Rosenfeld

J. E Ritter

M. R Lin



Available at: [https://works.bepress.com/thomas\\_lardner/1/](https://works.bepress.com/thomas_lardner/1/)

## Use of the microindentation technique for determining interfacial fracture energy

L. G. Rosenfeld, J. E. Ritter, T. J. Lardner, and M. R. Lin

Citation: *J. Appl. Phys.* **67**, 3291 (1990); doi: 10.1063/1.345363

View online: <http://dx.doi.org/10.1063/1.345363>

View Table of Contents: <http://jap.aip.org/resource/1/JAPIAU/v67/i7>

Published by the [American Institute of Physics](http://www.aip.org).

---

### Related Articles

Stress tunable properties of ferromagnetic microwires and their multifunctional composites

*J. Appl. Phys.* **109**, 07A310 (2011)

Spherical indentation of a finite poroelastic coating

*Appl. Phys. Lett.* **93**, 031911 (2008)

Analyses of the work required to delaminate a coating film from a substrate under oscillating load conditions and the film-substrate contact behavior after delamination

*J. Appl. Phys.* **103**, 103505 (2008)

A method to study the crack healing process of glassformers

*Appl. Phys. Lett.* **92**, 011918 (2008)

Time-resolved dynamic compaction and tensile fracture of low-porosity aluminum under impact loading

*J. Appl. Phys.* **102**, 073518 (2007)

---

### Additional information on J. Appl. Phys.

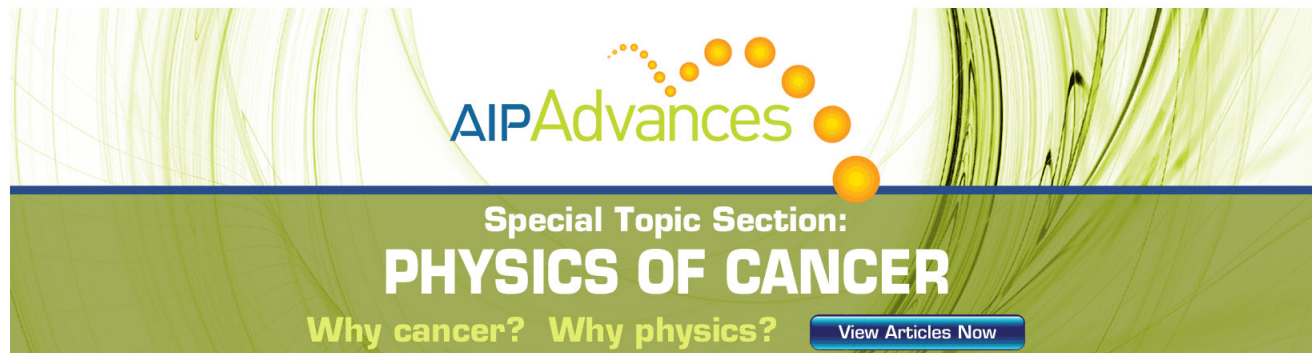
Journal Homepage: <http://jap.aip.org/>

Journal Information: [http://jap.aip.org/about/about\\_the\\_journal](http://jap.aip.org/about/about_the_journal)

Top downloads: [http://jap.aip.org/features/most\\_downloaded](http://jap.aip.org/features/most_downloaded)

Information for Authors: <http://jap.aip.org/authors>

## ADVERTISEMENT

The advertisement features a green background with abstract, flowing white and yellow lines. At the top, the "AIP Advances" logo is displayed, with "AIP" in blue and "Advances" in green, accompanied by a series of orange dots. Below the logo, the text "Special Topic Section:" is written in white, followed by "PHYSICS OF CANCER" in large, bold, white capital letters. At the bottom, the phrase "Why cancer? Why physics?" is written in yellow, and a blue button with the text "View Articles Now" is positioned on the right.

**AIP Advances**

Special Topic Section:  
**PHYSICS OF CANCER**

Why cancer? Why physics? [View Articles Now](#)

# Use of the microindentation technique for determining interfacial fracture energy

L. G. Rosenfeld, J. E. Ritter, T. J. Lardner, and M. R. Lin

Mechanical Engineering Department, University of Massachusetts, Amherst, Massachusetts 01003

(Received 28 September 1989; accepted for publication 18 December 1989)

The microindentation technique was used to determine the interfacial fracture energy of epoxy coatings on soda-lime glass substrates. An analytical model was developed for calculating fracture energy based on indenter load versus debond crack size measurements. Finite-element analysis was used to determine the relative amounts of opening and shear loadings at the debond crack tip. The calculated fracture energies are compared to values determined by the double-cantilever-beam technique and the four-point flexure-beam technique.

## INTRODUCTION

The microindentation technique for measuring adhesion of thin coatings consists of loading a coated surface with an indenter (ball or Vickers) until a critical load is reached to initiate an interface crack. Further loading of the indenter causes this interface crack to grow in a stable fashion. Thus the microindentation technique is unique in its ability to examine both the initiation and propagation stages of interfacial fracture. In a recent paper<sup>1</sup> the current authors developed a methodology for determining the interfacial shear stress to initiate debonding, i.e., interfacial shear strength, based on the measurement of the critical indenter load for initiating the interfacial crack.

The purpose of this paper is to present an analysis for determining the interfacial fracture energy based on the stable growth of the indentation-induced debond crack. A Griffith energy balance approach<sup>2</sup> is used to develop equations for determining interfacial fracture energy based on measurements of the debond crack size as a function of indenter load. A finite-element analysis is presented to verify the analytical model and give information on the relative amounts of opening and shear loadings at the crack tip. The results are compared to results obtained by the double-cantilever-beam method<sup>2-4</sup> and the four-point flexure-beam technique.<sup>5</sup>

## EXPERIMENT

The coated specimens for this study consisted of epoxy coatings (DGEBA epoxy resin with polyamide hardener) on soda-lime glass substrates. This coating/substrate combination was transparent, allowing direct observation of the debond crack during and after indentation. Prior to coating, the substrates were annealed at 520 °C for 24 h and cleaned in an ultrasonic methanol bath. The coatings for the indentation tests were deposited by a doctor blade technique to thicknesses ranging from 16 to 200  $\mu\text{m}$ . Curing was at room temperature as suggested by the manufacturer.

The indentation experiments were done with a Vickers indenter. The indenter was attached to a load cell which was bolted to the bottom of a universal testing machine crosshead. Specimens were placed coating side up on the stage of an inverted microscope that was positioned underneath the indenter to allow *in situ* viewing of the indentation. Indenta-

tions were made with a crosshead speed of 0.5 mm/min. A video recorder system was used to obtain indenter load versus debond crack size during the loading portion of the indentation cycle.

Double-cantilever-beam specimens [Fig. 1(a)] were fabricated with glass plates that had dimensions of 75 mm long by 12.5 mm wide by 1 mm thick. The 75 mm by 1 mm faces were polished with a cork belt and glued together with the epoxy adhesive to form the specimens. Note that the specimens were annealed after polishing and before gluing. A pair of holes were drilled at the end of each specimen to facilitate loading by a Universal testing machine. Precracks were put into the specimens by placing the specimens on a flat surface and applying a point load to the bondline near the loading holes. The precracks had lengths ranging from  $\frac{1}{4}$

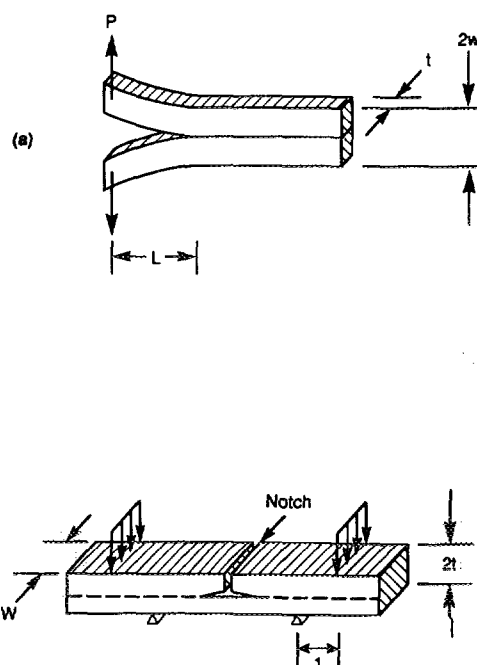


FIG. 1. Sketches of the (a) double-cantilever-beam specimen and (b) four-point flexure-beam specimens.

to  $\frac{1}{3}$  the length of the specimens. The specimens were loaded with a crosshead speed of 5 mm/min, and the failure loads were measured. The interfacial fracture energy was then calculated with the following equation<sup>3,4</sup>:

$$G_c = \frac{12P_c^2 L^2}{E_g t^2 w^3} [1 + 1.32w/L + 0.542(w/L)^2], \quad (1)$$

where  $G_c$  is the fracture energy,  $t$  is the specimen thickness,  $2w$  is the total specimen width,  $E_g$  is the elastic modulus of glass (70 GPa),  $L$  is the precrack length, and  $P_c$  is the fracture load.

For the four-point flexure-beam specimens, two annealed glass plates are glued together with the epoxy adhesive as shown in Fig. 1(b). The glass plates were 18.5 cm long by 2.5 cm wide. For two of the specimens, the glass plates were 5.5 mm thick, and for a third specimen the plates were 3 mm thick. After the epoxy adhesive had hardened, the edges of the specimens were ground with a belt sander to ensure that fillets of epoxy on the edges did not effect the crack growth behavior. The specimens were precracked by scribing a notch in the top layer of glass. Upon loading the specimen in three-point bending, a crack propagated downward from the notch and then branched symmetrically into the interface before arresting. The total length of the interfacial crack was controlled to be about 5 times the thickness of the upper glass plate. The precracked specimen was then placed in a four-point bending fixture (outer span = 10.2 cm and inner span = 6.4 cm) with the precracked side of the specimen on the tensile side and the interfacial crack tips within the inner loading span. Using a crosshead speed of 0.1 mm/min, the load for interfacial crack propagation was measured and the interfacial toughness was calculated based on<sup>5</sup>

$$G_c = (P_c^2 l^2 / 8E_g w) (1/I_2 - 1/I_c), \quad (2)$$

where  $P_c$  is the crack propagation load,  $l$  is one-half the dif-

ference between the inner and outer spans of the four-point bend fixture,  $w$  is the width of the glass plates,  $I_2$  is the moment of inertia of the single uncracked-beam, and  $I_c$  is the moment of inertia of the composite beam. The moment of inertia of the uncracked-beam is

$$I_2 = wt^3/12,$$

and the moment of inertia of the composite beam is

$$I_c = 2wt^3/3.$$

## ANALYSIS

Figure 2 shows a typical sequence of optical micrographs for a 105- $\mu$ m epoxy coating being indented with a Vickers indenter. It is seen that the debond crack forms in an annular region surrounding the central contact zone and extends stably during the loading portion of the indentation cycle. The cracks always extended in a smooth and continuous fashion with increasing indenter loads, and the deformations underneath the indenter were predominantly plastic since a permanent indent impression was left on unloading. Figure 3(a) contains a schematic of this indentation debonding. The deformations in the coating result in a radial stress underneath the indenter, which pushes outward on the surrounding debonded portion of the film.

An expression for the strain energy release rate can be obtained following Thouless<sup>6</sup> by modeling the debonded portion of the coating as an annular plate with plane stress conditions in the axial direction. Note that residual stress in and buckling of the coating are not accounted for in this model. We found that the epoxy coating had negligible residual stress, and a stability analysis of an annular plate shows that buckling does not occur. Figure 3(b) contains a schematic of the annular plate model. The stress distribution in the plate is determined by applying the Lamé equations with a zero-displacement boundary condition at the outer diame-

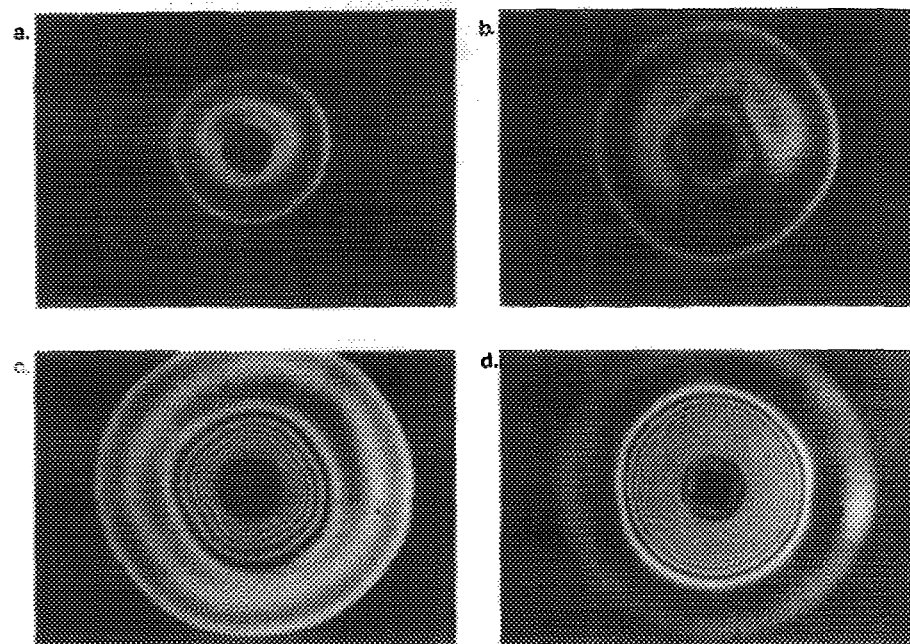


FIG. 2. Micrographs illustrating debonding by Vickers indentation of a 105- $\mu$ m epoxy coating. (a)  $P = 10$  N, (b)  $P = 20$  N, (c)  $P = 30$  N, and (d) unloaded.

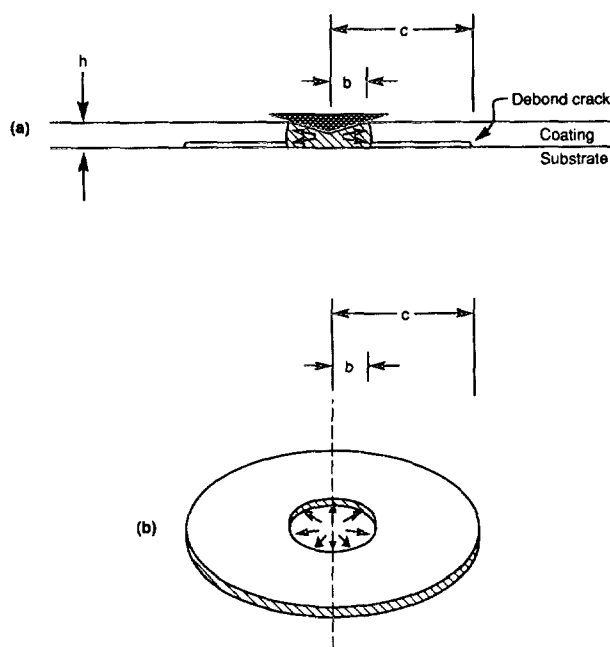


FIG. 3. (a) Schematic of indentation damage; (b) schematic of the annular plate model.

ter of the debond crack ( $r = c$ ) and a fixed radial stress  $\sigma_r$  at the inner diameter of the debond crack that is at the outer edge of the contact zone ( $r = b$ ). The zero-displacement boundary condition corresponds to the constraint provided by the surrounding adhered portion of the coating and the fixed stress corresponds to the pressure exerted by the central contact zone. The resulting stress distributions in the debonded portion of the coating are

$$\begin{aligned}\sigma_r &= \sigma_{rb} [1 + \alpha c^2/r^2] / [1 + \alpha c^2/b^2], \\ \sigma_\theta &= \sigma_{rb} [1 - \alpha c^2/r^2] / [1 + \alpha c^2/b^2],\end{aligned}\quad (3)$$

where  $b$  is the indenter contact radius,  $c$  is the crack radius,  $r$  is the radial position, the subscripts  $r$  and  $\theta$  refer to the radial and circumferential directions,  $\alpha$  is  $(1 - \nu_e)/(1 + \nu_e)$ , and  $\nu_e$  is Poisson's ratio of the epoxy coating. The strain energy in the plate ( $U$ ) is found by evaluating the following integral over the volume of the plate:

$$U = \frac{\pi h}{E_e} \int_b^c [\sigma_r^2 + \sigma_\theta^2 - 2\nu_e \sigma_r \sigma_\theta] r dr, \quad (4)$$

where  $E_e$  is the elastic modulus of the epoxy coating. The strain energy release rate ( $G$ ) (or the amount of energy available to form the two new surfaces as the crack extends) is found by differentiating the strain energy with respect to crack area,<sup>6</sup> with the result being

$$G = \frac{2(1 - \nu_e^2)\sigma_{rb}^2 h}{E_e} \left( \frac{1}{1 + \nu_e + (c/b)^2(1 - \nu_e)} \right)^2. \quad (5)$$

To determine  $G$  in terms of the indenter load  $P$ , rather than the indenter contact radius  $b$ , it will be assumed that the coating has a constant hardness, hence  $b = (P/2H)^{1/2}$ . The radial stress at  $r = b$ ,  $\sigma_{rb}$ , is found by applying the Tresca yield criteria to the plastically deformed contact zone. The vertical stress in this contact zone is equal to the mean in-

denter contact pressure, taken to be the hardness of the coating,  $H$ . From the Tresca yield criteria,  $\sigma_{rb}$  is then equal to  $(Y - H)$ , where  $Y$  is the yield stress of the coating in uniaxial tension. If the hardness of the coating is assumed to be  $2.25Y$ ,<sup>7</sup> then  $\sigma_{rb} = -0.56H$ . On making these substitutions for  $b$  and  $\sigma_{rb}$  into Eq. (5),

$$G = \frac{0.627H^2 h(1 - \nu_e^2)}{E_e} \frac{1}{[1 + \nu_e + 2(1 - \nu_e)Hc^2/P]^2}. \quad (6)$$

Equation (6) gives the critical strain energy release rate for crack propagation, i.e., the interfacial fracture energy  $G_c$ , when measured values of crack size as a function of indenter load are used. If  $H$  and  $G_c$  are independent of indenter load and crack length, Eq. (6) predicts that crack length should be proportional to the indenter load to the  $1/2$  power.

To further understand the crack driving forces, finite-element analysis was applied to the annular plate model depicted in Fig. 3(b). The analysis was performed with the ANSYS finite-element program using eight-noded isoparametric elements. The axisymmetric mesh used for this analysis is shown in Fig. 4. The applied stress and displacement boundary conditions are shown in Fig. 4. The applied stress at the inner edge of the coating ( $r = b$ ) was 100 MPa. For the soda-lime glass substrate,  $E_g = 70$  GPa and  $\nu_g = 0.25$ , and for the epoxy coating  $E_e = 3.60$  GPa and  $\nu_e = 0.38$ . Quarter-point elements were placed at the crack tip to produce a square-root singularity in the stress field at the crack tip as an approximation to the stress singularity at the bimaterial interface.<sup>2</sup> The mesh in Fig. 4 was modified by adding or subtracting elements from the loaded edge of the coating at  $r = b$  so that results were obtained for three different values of the ratio  $c/b$ : 1.68, 2.46, and 4.57. An additional analysis was performed for  $c/b = 2.46$  with a finer mesh to insure that the solution was convergent.

The output of the finite-element analyses consisted of nodal displacements. Figure 5 contains a plot of the distorted mesh for  $c/b = 2.46$ . It is seen that there is a gap between the coating and the substrate. This is in agreement with the experimentally observed interference pattern that shows that the coating lifts off the substrate above the debond region. Based on the crack opening displacements for the first

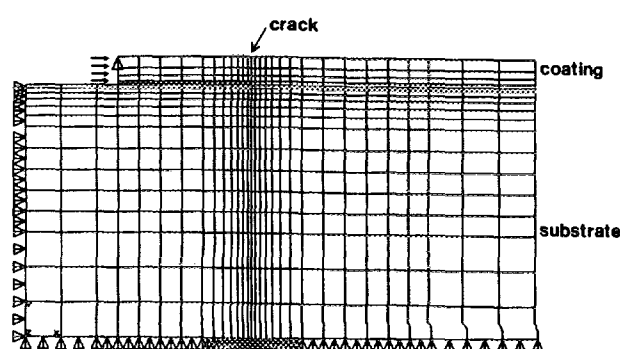


FIG. 4. The axisymmetric mesh that was used for finite-element analysis. The triangles refer to displacement boundary conditions, and the arrows refer to applied stresses.

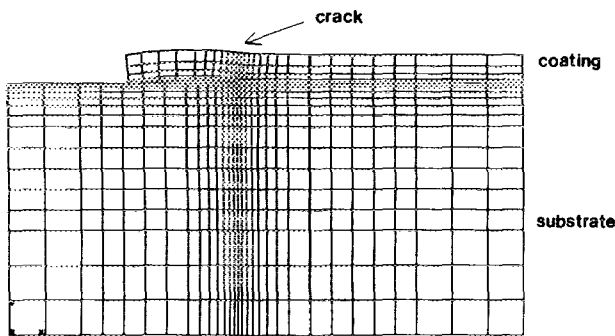


FIG. 5. The displaced configuration of the finite-element mesh for  $c/b = 2.46$ .

four nodes adjacent to the crack tip, the average strain energy release rate for the three values of  $c/b$  were calculated with the following equation<sup>8-10</sup>:

$$G = \frac{2\pi\lambda^2(u^2 + v^2)}{(\Lambda_c + \Lambda_g)r}, \quad (7)$$

where  $v$  and  $u$  are the crack opening displacements in the opening and shearing modes, respectively, from nodes along the crack surfaces,  $r$  is the distance between the nodes and the crack tip in the undeformed mesh, and the terms  $\lambda$  and  $\Lambda$  are given by

$$\Lambda = 4(1 - \nu)/\mu, \quad (8a)$$

$$\lambda^2 = (1 + 4\epsilon^2)/4, \quad (8b)$$

where  $\mu$  is the shear modulus of glass or epoxy, and  $\epsilon$  is given by

$$\epsilon = \frac{1}{2\pi} \ln \frac{1 - \beta}{1 + \beta},$$

and

$$\beta = \frac{\mu_g(1 - 2\nu_c) - \mu_c(1 - 2\nu_g)}{2[\mu_g(1 - \nu_c) + \mu_c(1 - \nu_g)]}.$$

Equation (7) is derived directly from the displacement field at the tip of a crack at a bimaterial interface and was originally applied to finite-element results by Liechti and Hanson.<sup>8</sup> In Fig. 6 the calculated values of  $G$  are compared in normalized form to the prediction of Eq. (5). To normalize the finite-element results, the elastic modulus of the epoxy coating was used (3.6 GPa). It is seen that the agreement between the finite-element and the analytical solution is quite good. It is also evident that the strain energy release rate decreases as the crack extends, in agreement with the observed stable crack growth.

## RESULTS

Figures 7 and 8 contain plots of the measured coating hardness and the debond crack size as a function of indenter load. With both sets of data there is some scatter, especially for low indenter loads and thin coatings. This scatter is due to the increased uncertainty in the contact diagonal and debond crack size measurements at low loads with thin coatings. Nevertheless, it is evident that the coating hardness (Fig. 7) is essentially independent of indenter load, con-

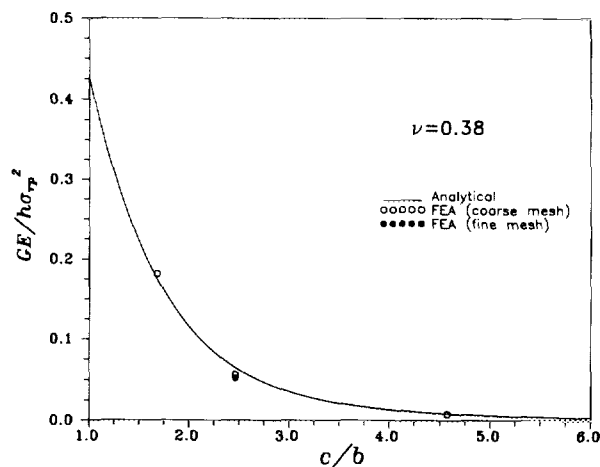


FIG. 6. Comparison of the normalized strain energy release rate as a function of the ratio  $c/b$  from analytical model and finite-element analysis.

tent with the assumption used in deriving Eq. (6), and that the observed relation between indenter load and crack size (Fig. 8) is in good agreement with the predicted trend of Eq. (6),  $c \propto P^{1/2}$ . Values of the interfacial fracture energy for each data point in Fig. 8 were determined using Eq. (6). For all thicknesses the elastic modulus of the epoxy coating was taken to be 3.6 GPa, Poisson's ratio 0.38, and the coating hardness 238 MPa. The average and standard deviation of the interfacial fracture energy values for each thickness are shown in Fig. 9. While there is some scatter in these results, the interfacial fracture energies are independent of thickness with an average value of  $25.2 (\pm 8.7) \text{ J/m}^2$ .

Interfacial fracture energies measured by the double-cantilever-beam technique are shown in Fig. 10 as a function of the initial precrack length. The measured values are independent of precrack length with an average value of  $8.1 (\pm 1.7) \text{ J/m}^2$ . In the four-point flexure-beam test, the debond crack growth was accompanied by load discontinuities associated with initial crack growth followed by arrest. A typical load versus crosshead displacement curve is shown

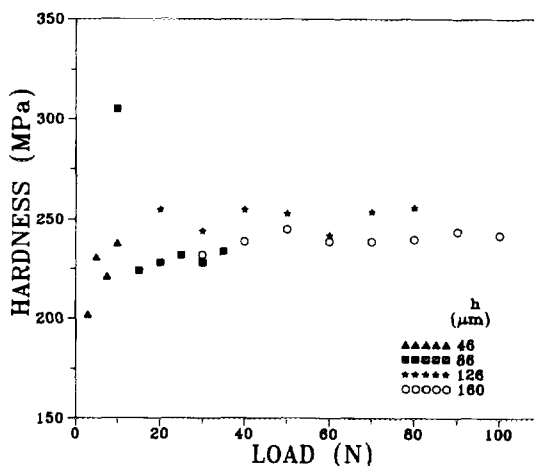


FIG. 7. Hardness of the epoxy coatings on soda-lime glass substrates as a function of indenter load.

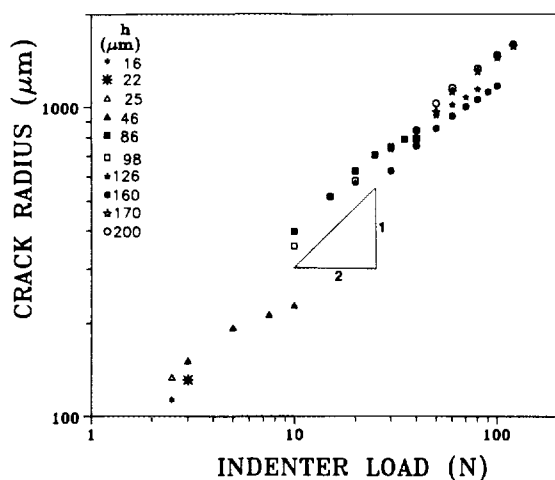


FIG. 8. Debond crack radius as a function of Vickers indenter load.

in Fig. 11. Based on the average of the peak load values for the three specimens, the critical energy release rate for crack propagation  $G_c$  was determined to be  $15.0 (\pm 0.4) \text{ J/m}^2$ .

The differences in the interfacial fracture energies measured by the three techniques can be attributed to the different relative amounts of mode-I (opening) and mode-II (shearing) crack loadings in the three specimens. The relative amounts of mode-I and mode-II loading in a given test can be quantified by the phase angle which for small  $\epsilon$  is approximately  $\tan^{-1} (u/v)$ .<sup>5,11</sup> For the epoxy/glass interface studied here,  $\epsilon$  is equal to 0.056. Note that a phase angle of  $0^\circ$  corresponds to pure crack opening loading, while a phase angle of  $90^\circ$  corresponds to pure shear loading. Values of the phase angle associated with the microindentation test were calculated from the crack opening displacement for each value of  $c/b$ . In Fig. 12 the calculated values of phase angle are plotted as a function of  $c/b$ . It is seen that the phase angle varies from  $45^\circ$  to  $55^\circ$ , depending on the crack size. Since the ratio  $c/b$  for the data in Fig. 8 was between 2 and 3, the phase angle for the indentation results is about  $54^\circ$  based on the results in Fig. 12. For the double-cantilever test, the specimen is subjected to pure mode I loading so that the

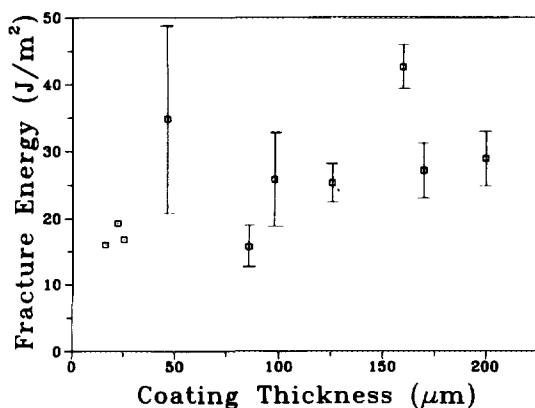


FIG. 9. Calculated interfacial fracture energies as a function of coating thickness based on indentation experiments.

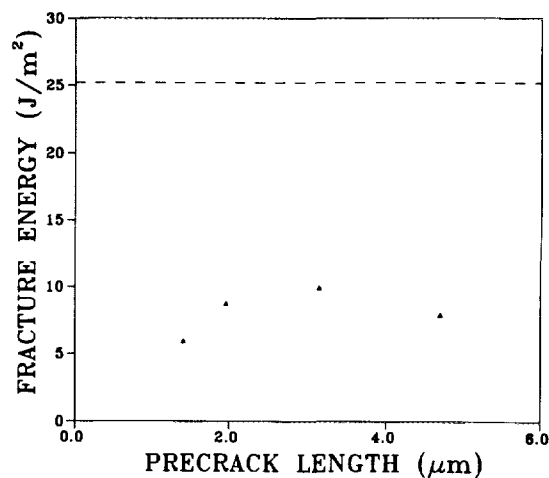


FIG. 10. Measured interfacial fracture energies as a function of precrack length from the double-cantilever-beam test. The dashed line indicates the average value obtained from indentation (Fig. 9).

phase angle is  $0^\circ$ . For the four-point flexure-beam test the phase angle has been determined to be  $41^\circ$ .<sup>5</sup> In Fig. 13 the interfacial fracture energies from the three different tests are plotted as a function of phase angle. The observation of increased fracture energy with mode-II loadings, which is seen in Fig. 13, has been made by many researchers.<sup>2,5,12-14</sup> In one particular study,<sup>5</sup> a phase angle versus fracture energy curve similar to Fig. 13 was measured in a system consisting of a thermoplastic adhesive bonded to glass. In this case the authors concluded that the increase in fracture energy with phase angle could be due to crack tip plasticity and a non-planar interface.

The absolute values of interfacial fracture energy measured in this study can be compared to values obtained by Liechti and Hanson<sup>8</sup> for an epoxy system consisting of a modified bisphenol A resin with an amido amine hardener and soda-lime glass substrates. Using a blister test, which has a phase angle of about  $33^\circ$ , the interfacial fracture energy was found to be about  $33 \text{ J/m}^2$ , which is similar to the values found in this study.

It should be noted that the model presented in this paper for indentation induced debonding of soft compliant coatings on rigid substrates differs significantly from that devel-

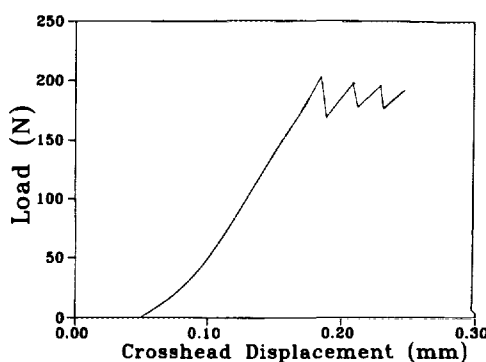


FIG. 11. Load vs crosshead displacement from the four-point flexure-beam test.

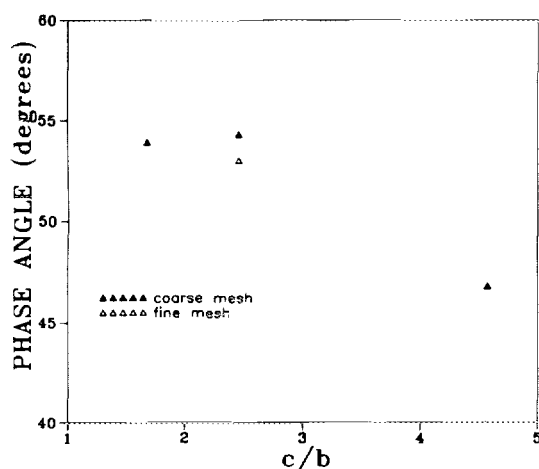


FIG. 12. Phase angle associated with the indentation-induced debond crack as a function of crack radius.

oped for coatings having similar elastic properties to the substrate.<sup>15,16</sup> This latter model assumes that the driving force for an interfacial crack is the residual indentation stresses that arise on unloading, whereas the model presented herein assumes that the debond crack is driven by contact stresses on loading. The model based on residual indentation stresses predicts that the dependency of the debond crack size on indenter load is to the  $\frac{3}{4}$  power rather than the  $\frac{1}{2}$  power which is predicted for debond cracks driven by contact stresses. Clearly, the data for a soft compliant coating on a rigid substrate (Fig. 8) agrees with the contact stress model.

## SUMMARY

A methodology has been developed whereby mixed-mode interfacial fracture energies of thin polymer coatings can be measured by the microindentation technique. The analysis was confirmed with finite-element analysis and experiments on a model system consisting of epoxy coatings on soda-lime glass substrates. The microindentation technique has three main advantages over conventional techniques. First, there is no special sample size or geometry restrictions. Second, the indentation-induced debond crack grows in a stable fashion so that multiple measurements can be made on a single specimen. Third, and most importantly, the technique can be used to determine both the interfacial shear

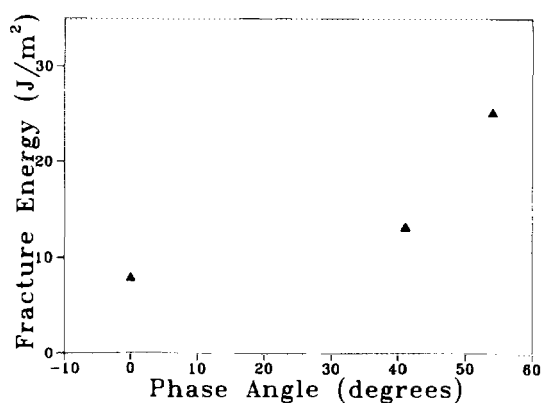


FIG. 13. Measured interfacial fracture energies as a function of phase angle for epoxy/soda-lime glass system.

strength associated with crack initiation<sup>1</sup> and the interfacial fracture energy associated with crack propagation.

## ACKNOWLEDGMENT

This research was supported by an IBM Materials and Processing Sciences grant to the Institute of Interface Science at the University of Massachusetts, Amherst, MA.

- <sup>1</sup>J. E. Ritter, T. J. Lardner, L. Rosenfeld, and M. R. Lin, *J. Appl. Phys.* **66**, 3626 (1989).
- <sup>2</sup>A. J. Kinloch, *Adhesion and Adhesives* (Chapman and Hall, New York, 1987).
- <sup>3</sup>F. P. Champonier, in *Fracture Mechanics Applied to Brittle Materials*, edited by S. W. Freiman, ASTM STP 678 (ASTM, Philadelphia, 1979), p. 60.
- <sup>4</sup>S. W. Weiderhorn, A. M. Shorb, and R. L. Moses, *J. Appl. Phys.* **39**, 1569 (1979).
- <sup>5</sup>H. C. Cao, B. J. Dagleish, and A. G. Evans, *Closed Loop* **17**, 19 (1989).
- <sup>6</sup>M. D. Thouless, *Acta. Metall.* **36**, 3131 (1988).
- <sup>7</sup>D. M. Marsh, *Proc. R. Soc. London A* **279**, 420 (1964).
- <sup>8</sup>K. M. Liechti and E. C. Hanson, *Int. J. Fract.* **36**, 199 (1988).
- <sup>9</sup>R. E. Smelser, *Int. J. Fract.* **13**, 382 (1977).
- <sup>10</sup>B. M. Malyshev and R. L. Salganik, *Int. J. Fract.* **27**, 114 (1965).
- <sup>11</sup>J. R. Rice, *J. Appl. Mech.* **55**, 98 (1988).
- <sup>12</sup>G. P. Anderson and K. L. DeVries, *J. Adhes.* **23**, 289 (1987).
- <sup>13</sup>G. P. Anderson, K. L. DeVries, and M. L. Williams, *J. Colloid Interface Sci.* **47**, 600 (1974).
- <sup>14</sup>G. G. Trantina, *J. Compos. Mater.* **6**, 371 (1972).
- <sup>15</sup>D. B. Marshall and A. G. Evans, *J. Appl. Phys.* **56**, 2632 (1984).
- <sup>16</sup>C. Rossington, A. G. Evans, D. B. Marshall, and B. T. Khuri-Yakub, *J. Appl. Phys.* **56**, 2639 (1984).